Modeling and Control of a Dual Cell Link for Battery-Balancing Auxiliary Power Modules

Weizhong Wang and Matthias Preindl
Department of Electrical Engineering, Columbia University in the City of New York
New York, NY 10027, USA

***Abstract*—This paper focuses on the design of current controllers of a half-full bridge balancing link for a battery-balancing auxiliary power module. The fundamental concept of the converter is explained, e.g. phase shift control. For steady-state operation while the cells are unbalanced, a duty cycle adjustment is introduced to make inductor VA balanced. The proposed topology offers four typical balancing modes, including cells to auxiliary, cell to cell and auxiliary, auxiliary to cells, and cell to cell. They are realized by properly controlling leakage inductor current and output power from the half-full bridge. The average model of the topology and the linearized output power characteristic are derived to help choose the current controller gains. High-fidelity validation results are shown to verify the controller design and mode switching given the cell current demands.**

I. Introduction

Electrified vehicles (EVs) are the most promising technologies to reduce the carbon footprints. As the main power source in EVs, batteries are the biggest concern in terms of energy density and efficiency [1]. Due to internal and external factors of battery, such as impedance differences from manufacturing and inconsistent distributions of thermal energy over the battery pack, battery cells become unbalanced during operation. Therefore, battery balancing is regarded as a means to increase power efficiency and cruise range [2].

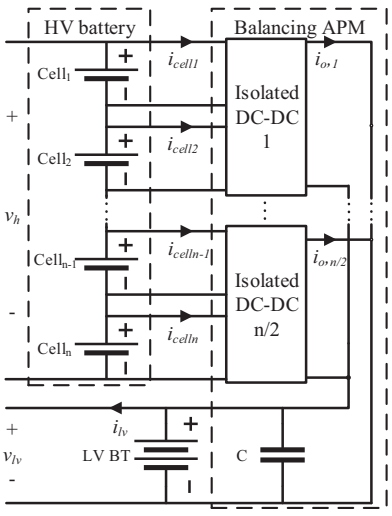

Fig. 1. Block diagram of APM balancing circuit

Passive balancing and non-dissipative balancing are the two main categories: the former dissipates the energy with resistors [3], the latter is proved to be the more efficient approach by shunting the energy from stronger cells to weaker cells, especially when cell to stack and stack to cell are enabled [4]. However, the non-dissipative technique is rarely applied in practice due to the cost. Therefore, a novel auxiliary power module (APM) based balancing topology has been proposed to reduce the cost [5], [6], as shown in Fig. 1, which simultaneously realizes conversion from high voltage (HV) to low voltage (LV) and balancing functionality.

Many power DC-DC converters can be applied in this APM balancing circuit, as long as they are bi-directional and isolated. For higher efficiency and smaller size, soft switching, high-frequency operation and less power switches are preferred. The theory has been investigated by a dual active bridge (DAB) technique as the power electronics medium from HV to LV [6]. The design fulfilled the purpose of balancing and voltage level conversion, but it is hard to be convinced as a compact or cost-friendly design due to a large number of power switches used (8 switches for balancing one battery cell) in DAB.

Therefore, in this paper a half-full bridge (HFB) topology exclusively for battery balancing application is proposed to reduce the number of switches (3 switches for balancing one battery cell) and offers an extra cell-to-cell current flow direction to increase the balancing speed. An undesired phenomenon in other applications has been strategically utilized to realize power transfer between cells. The paper is organized as follows, Section II explains the basic concept and modeling of the HFB topology. The controller to reference cell currents is described and designed in Section III. The validation results and conclusions are given in Section IV and V, respectively.

II. HFB Topology and Average Modeling

The proposed isolated HV-LV converter consists of a half bridge on the primary side (PS) and a full bridge on the secondary side (SS), as shown in Fig. 2. The half bridge lets two cells connected in one converter. On the other hand, the full bridge offers more reliable and stable voltage on the SS. The high frequency transformer in between is responsible for energy transfer and isolation. By replacing input filtering capacitors on the half bridge with two battery cells, the proposed topology is capable of HV-LV conversion and battery balancing. To simplify the analysis in this study, LV battery and loads are represented by a current source.

A. Basic Control Logic

The phase shift control is adopted in this study to enable bi-directional power flow [7]–[9]. Introducing a leading phase

978-1-5386-1180-7/18/$31.00 ©2018 IEEE

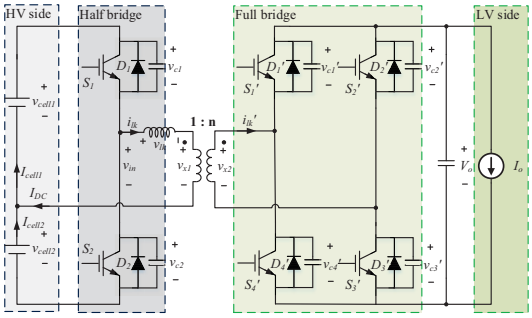

Fig. 2. The HF topology applied in APM

d between PS and SS switches leads to positive power flow (HV to LV), and vice versa.

However, the duty cycles of high-side S_1 and low-side S_2 are both 50% in phase shift control for the PS, also known as symmetric control. Less than 50% duty cycle can also be used in phase shift control, but the 50% duty cycle enables the largest output power range since higher phase shift can be applied. It is because the phase shift is proportional to output power in this type of control [10]. Note that the phase shift control cannot be directly applied to the proposed topology since the two cells on the PS are normally unbalanced in terms of SOC and voltage, if without proper BMS. A simple observation can be made by KVL: the voltage on the leakage inductance has the following format:

$$v_{lk,n} = v_{cell,n} - v_{x1} \tag{1}$$

where the subscript $n \in [1, 2]$ in $v_{lk,n}$ and $v_{cell,n}$ indicates the index of the battery cell(s) that is currently conducting. Note that the cell voltage changes are barely noticeable when the switching frequency is high, e.g. 10 MHz. As a result, the battery cells are treated as a constant voltage source with voltage $V_{cell,n}$ within a switching period. v_{x1} is the output voltage referred to PS, which is also assumed to be constant if output capacitor is big enough. Therefore, the inductance current changes at a rate of $v_{lk,n}/L_{lk}$, which differs when the two cells have different voltage level, i.e. unbalanced.

The waveforms of current and voltage for the leakage inductance can be depicted in Fig. 3, under the condition where $V_{cell1} > V_{cell2}$. Two situations are included: symmetric control and asymmetric control, which are drawn by red dotted line and black line in Fig. 3 (c), respectively. As discussed above, the imbalance of cell voltages causes the VA imbalance of leakage inductance if symmetric control is applied, i.e. the average current on the leakage inductance is not zero within one period. Consequently, the drifting leakage inductor current is observed, as shown by red dotted line in Fig. 3 (c). The uncontrolled average current causes many consequences, such as flux saturation and overheating.

To compensate the VA imbalance, an asymmetric control is proposed by introducing a duty cycle adjustment θ on the PS switches. This adjustment is simply tuning the conducting time for each cell based on their voltages. For example, if cell 1 has higher voltage, its duty cycle will be set to 50% - θ and cell 2 will have a complementary conducting time of 50% + θ, as shown in Fig. 3 (a). It guarantees the accumulative effects of two cells on the leakage inductor are identical. Combining the phase shift control and the asymmetric control enables bi-directional power flow and balanced VA of the leakage inductance.

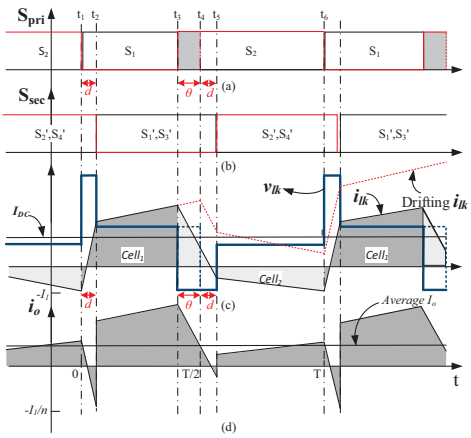

Fig. 3. The waveforms of operating half-full bridge converter without asymmetric control (red dot), and with asymmetric control (black line)

The duty cycle adjustment can be obtained by letting $i_{lk}(0) = i_{lk}(T)$ in one period, as shown in (2). That is, the net change of the inductor current over a full period is zero.

$$\theta = \frac{T}{2}\left(\frac{V_{cell1} - V_{cell2}}{V_{cell1} + V_{cell2}}\right) = \frac{T}{2}\frac{\Delta V}{V_{DC}} \tag{2}$$

where, the cells' voltages v_{cell1} and v_{cell2} are approximated as constant V_{cell1} and V_{cell2} due to their slower variation at high frequency, as discussed previously.

It can be seen from (2) that the duty cycle adjustment θ is a function of the voltage difference and summation of the two cells in one HF. Note that the phase shift d is set to be the same for both S_1 and S_2.

B. Average Modeling for Leakage Inductor Current

In order to establish the system model to employ control algorithms, average modeling technique is adopted. The averaged dynamic behavior can be mathematically modeled and the averaged variables are exactly desired, such as the averaged output current and DC offset current for the leakage inductor.

By assuming small ripples in the waveforms of inductors or capacitors, the instantaneous values are replaced by their low-frequency averaged values denoted as a 'bar' over the corresponding instantaneous values, e.g. $\bar{i}_{lk}(t)$.

The inductor voltage by definition is:

$$v_{lk}(t) = L\frac{di_{lk}(t)}{dt} \tag{3}$$

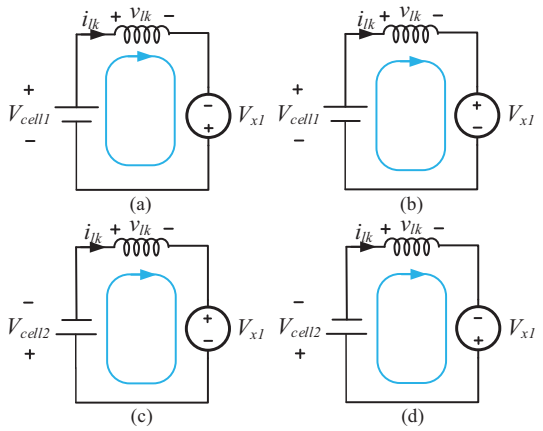

Fig. 4. Equivalent circuit models referred to primary side during: (a) $0 \leq t < d$, (b)$d \leq t < \frac{T}{2}$, (c) $\frac{T}{2} - \theta \leq t < \frac{T}{2} + d$, and (d)$\frac{T}{2} + d \leq t < T$

The voltage can be divided to four subintervals within one period. The equivalent circuit models and expressions within each subinterval are given in Fig. 4 and (3), respectively.

$$\bar{v}_{lk}(t) = \begin{cases} V_{cell1} + V_{x1}, & t \in [0, d] \\ V_{cell1} - V_{x1}, & t \in [d, \frac{T}{2} - \theta] \\ V_{cell2} + V_{x1}, & t \in [\frac{T}{2} - \theta, \frac{T}{2} + d] \\ V_{cell2} - V_{x1}, & t \in [\frac{T}{2} + d, T] \end{cases} \tag{4}$$

where V_{x1} is output voltage referred to primary side through the transformer, which is considered as constant voltage source with voltage V_o/n V. So the average voltage during each subinterval is constant if cell voltages and V_{x1} are assumed constant.

Therefore, the average voltage during the entire period can be obtained:

$$\begin{aligned} \bar{v}_{lk}(t) &= \frac{1}{T}\int_{t}^{t+T} v_{lk}(t)dt \\ &= \frac{1}{T}[d(V_{cell1} + V_{x1}) + (\frac{T}{2} - \theta - d)(V_{cell1} - V_{x1}) \\ &\quad + (d + \theta)V_{cell2} + V_{x1} + (\frac{T}{2} - d)(V_{cell2} - V_{x1})] \\ &= \frac{1}{2}[(V_1 - V_2) - \theta(t)(V_1 + V_2)] \end{aligned} \tag{5}$$

Insertion of this equation into (3) leads to

$$L\frac{d\bar{i}_{lk}(t)}{dt} = \bar{v}_{lk}(t) = \frac{1}{2}[(V_1 - V_2) - \theta(t)(V_1 + V_2)] \tag{6}$$

This equation describes how the low-frequency components (simply DC component in our case) of the inductor current vary with time. It shows that the dynamic of the leakage inductor current is purely a function of duty cycle adjustment θ, which implies the average leakage inductor current is controllable by varying θ.

It can be observed from Fig. 2 that the average leakage inductor current $\bar{i}_{lk}(t)$, for clearer presentation denoted as I_{DC}, is actually the difference between two cells' average currents. It is because the high frequency current component is transferred through the transformer to the SS and DC offset remains on the PS. Therefore, controlling the DC offset current I_{DC} regulates the difference between cell currents. Note that this matches the concept of battery balancing, which distributes the current demands on each cell according to corresponding SOCs/Voltages.

C. Output Characterization

Considered as nominal battery voltage, output voltage is modeled as a constant voltage source. Therefore, output current determines the level of output power. Besides, output current/power is approved to be an intermediate controllable variable in the following section. Therefore, finding an expression of output current is beneficial for our control algorithm.

Working like a rectifier, the full-bridge regulates current to remain positive polarity as long as possible. Also, based on the phase shifted gate signals, the waveform of the output current is drawn in Fig. 3 (d). It is redrawn in Fig. 5 for better and clearer explanation.

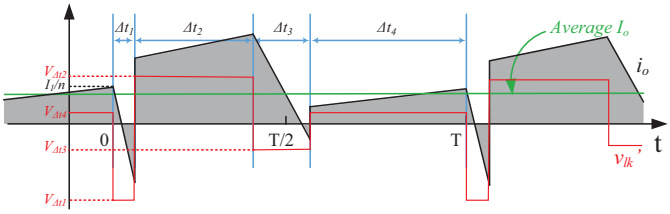

Fig. 5. Instantaneous and average output currents, and corresponding leakage inductor voltage on secondary side

The average output current can be obtained by calculating the area under the current waveform, as shown by shaded area in Fig. 5. Due to nearly constant voltage drop over the leakage inductor on SS, the current waveform can also be divided into four piece-wise linear subintervals, i.e. $\Delta t_1, \Delta t_2, \Delta t_3$, and Δt_4, as shown in Fig. 5. The average output power from HFB can be derived as follows:

$$\begin{aligned} P_o = V_o I_o &= \frac{V_o}{T}\int_0^T i_o(t)dt \\ &= \frac{V_o T}{8L_{lk}n}[V_{cell1}\alpha_1 + V_{cell2}\alpha_2] \end{aligned} \tag{7}$$

and

$$\begin{aligned} \alpha_1 &= -1 + 4d' + 4\theta' - 2d'^2 - 4\theta'^2 - 8d'\theta' \\ \alpha_2 &= 1 + 4\theta' - 2d'^2 - 4\theta'^2 - 8d'\theta' \end{aligned} \tag{8}$$

where normalized duty cycle adjustment θ' and phase shift d' are calculated by $x' = x/(T/2)$. The equation yields the same results when two cells are balanced as other researchers claim for DAB and DHB topologies, i.e. $V_{cell1} = V_{cell2}$. It indicates (7) is a generalized expression for output power in DAB and DHB topologies, regardless of the conditions of the input voltage sources.

III. Lower-level Controller Design

The APM balancing circuit is controlled by global balancing controller which determines the balancing current distribution of the HV cells based on their SOCs or voltages, as shown in Fig. 6. Each lower-level controller is responsible for regulating the current demand between two cells in one HFB. The proposed topology is compatible with typical balancing control algorithms. In this paper, we assume the balancing control algorithm in [5] is used. This algorithm issues a required balancing current that is actuated as current reference in the proposed topology.

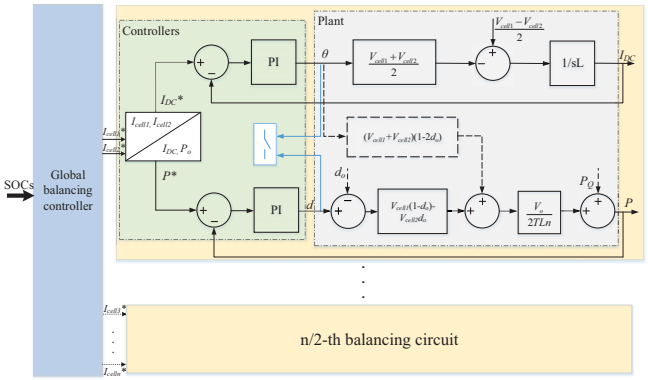

Fig. 6. Diagram of lower-level controller

A. Reference Translation

However, cell currents I_{cell1} and I_{cell2} cannot be directly controlled since they do not have a direct relationship with the controllable variables θ and d. It is observed that DC offset current I_{DC} and output power P_o are linked with θ and d in (6) and (7). An intermediate transformation is needed from cell currents to the controllable variables.

In the lossless case, input power is 100% transferred to output or the cells to be charging, which yields $P_o = P_{in} = V_{cell1}I_{cell1} + V_{cell2}I_{cell2}$. Therefore, given $I_{DC} = I_{cell1} - I_{cell2}$, the intermediate transformation matrix is derived as $\mathbf{T}$:

$$\begin{bmatrix} I_{DC} \\ P_o \end{bmatrix} = \mathbf{T} \begin{bmatrix} I_{cell1} \\ I_{cell2} \end{bmatrix} = \begin{bmatrix} 1 & -1 \\ V_{cell1} & V_{cell2} \end{bmatrix} \begin{bmatrix} I_{cell1} \\ I_{cell2} \end{bmatrix} \tag{9}$$

Consequently, in the lower-level controller, the reference of current distribution generated by the global controller is translated to the reference of I_{DC} and P_o by the transformation matrix $\mathbf{T}$.

B. Linearized Power Characteristics

It is observed that (7) has two controllable variables coupling together, which makes controllers hard to be designed and implemented. A reasonable method to decouple the nonlinear relationship is Taylor series expansion, which is used to linearize the expression in (7) around a quiescent point Q:

$$\begin{aligned} P_o =& P_o|_{\theta'_Q, d'_Q} + \frac{V_o T}{2L_{lk} n}[(V_{cell1} + V_{cell2})(1 - 2d'_Q)\theta' \\ &+ (V_{cell1}(1 - d'_Q) - V_{cell2} d'_Q)(d' - d'_Q)] \end{aligned} \tag{10}$$

where θ'_Q and d'_Q are quiescent operation points. They are normally set to be the steady-state conditions. θ is given by (2) which leads to a balanced leakage inductor current, and d'_Q is determined to deliver a certain level output power based on (7). A linearized power curve is compared with the original power curve in Fig. 7 for a specific circuit design, cell voltage and power levels, but it is general for other conditions.

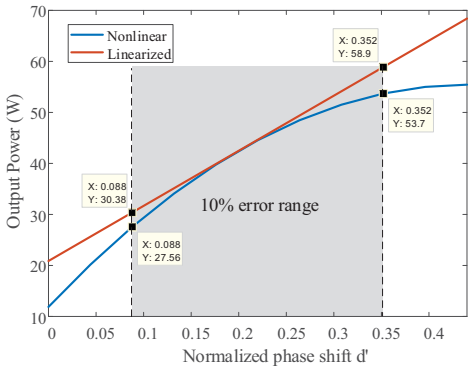

Fig. 7. Comparison between linearized and original power curves

The plot shows the linearized power at $d'_Q = 0.2$ has less than 10% error in a large phase shift range, varying from 0.09 to 0.352. It covers the majority of area if 40 W output power is required. Obviously, d'_Q can be selected accordingly if the power range is required narrower. This result will give enough information for intelligent controllers to react accurately.

C. Overall Control Strategy

Based on (6) and (10), the diagram of lower-level controller is depicted by the green block in Fig. 6. Two reference currents for the corresponding cells in one HFB device are fed into the lower-level controller. After translating them into reference DC offset current and output power, the measurements are compared and their error signals are transmitted to two PI controllers. The two control variables from PI controllers are driving the gates of the switches to realize the control process.

The dashed block between duty cycle adjustment and phase shift PI controllers is cross-coupling term from θ. One can design a PI controller to compensate those terms; however, in this study, those terms are treated purely as disturbances and the PI controller is considered robust to eliminate the disturbances in closed-loop control. Therefore, only forward path is concerned when designing the PI controllers.

Bode plots are applied to sketch the design of two PI controllers. It is noted that if the compensator gain at the switching frequency is too great, then these switching harmonics are amplified by the compensator, and can disrupt the operation of the PWM [11]. Normally 10 % of switching frequency is preferred, e.g. cutoff frequency at 1 MHz if switching at 10 MHz. For the PI controller of θ, it can be obtained from the block diagram in Fig. 6 that the transfer function of the open-loop system is:

$$G_1 = G_{PI_1} G_\theta = -\frac{K_P s + K_I}{s} \frac{V_{cell1} + V_{cell2}}{2L_{lk} s} \tag{11}$$

The Bode plot of G_1 with gain and phase margins is shown in Fig. 8, where K_P and K_I are given in Table I. The two extreme conditions are included: $\max\{V_{cell1} + V_{cell2}\} = 2V_{cellmax}$ and $\min\{V_{cell1} + V_{cell2}\} = 2V_{cellmin}$. It can be seen from the Fig. 8 that gain and phase margins deviate insignificantly; so that the open-loop system has a nearly constant cutoff frequency at 1 MHz while the system is switching at 10 MHz. The same analysis can be also applied to the second PI controller; the PI gains of the output power controller are given in Table I.

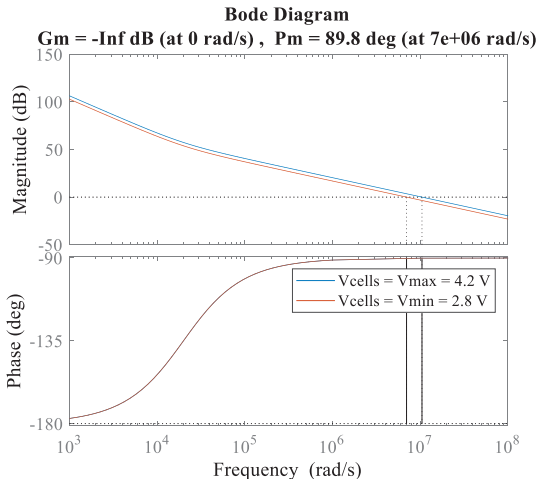

Fig. 8. The Bode plot for the PI controller of θ

IV. Results

The average model is validated with the detailed model at 10 MHz. The parameters for validation purpose are given in Table I. At 2×10^{-6} s, the duty cycle adjustment step increases from $0.9\theta_0$ to θ_0, where θ_0 is the balanced duty cycle adjustment given in (2), as shown in Fig. 9. The step increase drives the unbalanced leakage inductance current back to balanced one so that the transient states can be captured. The result demonstrates that average and detailed models match very well. The upper and lower envelopes predicted by average modeling track the instantaneous responses accurately as well. It proves that the average model is able to represent the dynamics and steady-state behavior.

TABLE I
Simulation Parameters of the Proposed HFB Topology

Switching frequency (MHz)	10
Turns Ratio	1:5
Leakage inductance (nH)	2
Output filtering capacitor (uF)	3
Cell voltages (V)	Cell1: 4.2 Cell2: 3.3
Gains of PI 1	$Kp = 5\times10^{-3}$ $K_I = 10^3$
Gains of PI 2	$Kp = 10^{-3}$ $K_I = 10^4$

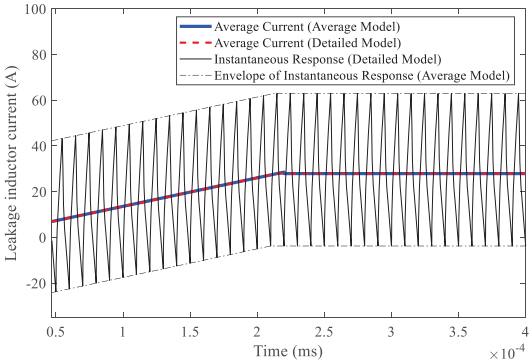

Fig. 9. The comparison between detailed model and average model

The second test is aiming at testing all possible operating conditions and their transient response from one to another. As the cells balance/deviate, the reference current distribution is adjusted by the global controllers frequently to either meet the output or speed up balancing process. The possible current distribution includes (i) cell 1 and cell 2 are charging (negative currents), (ii) cell 1 is discharging while cell 2 is charging ($I_{cell1} > 0$ and $I_{cell2} < 0$), and (iii) both cells are discharging ($I_{cell1}, I_{cell2} > 0$).

TABLE II
References for Test Conditions

Condition #	1	2	3	4
Cell Currents (A)	5 and 3	5 and -2	-2 and -6	5 and -5
Voltages (V)	Cell 1: 4.2 Cell 2: 3.3			
Output Power (W)	30.9	14.4	-28.2	0

Four operation modes with specific current demands, as listed in Table II, are verified in Fig. 10. At first, the balancing system is given with current references 5 A and 3 A from cell 1 and cell 2, respectively, which yields 30.9 W output power to auxiliary, the same with previous analysis in lossless cases. Adjusting d' and θ', the controllers converge to the correct references swiftly and accurately, as shown in Fig. 10 (a).

Once the system operates in steady state, the current references step change to 5 A and -2 A at approximately 250 μs. Output power of 14 W is generated with the new current demand. Positive power flow leads to positive phase shift. Therefore, d' decreases to a smaller value that can be calculated based on power level by (7) than previous d' . On the other hand, θ' just subtly fluctuates around previous steady-state condition to reach the new level of leakage inductor current, i.e. $I_{DC} = I_{cell1} - I_{cell2} = 5-3 = 2A \rightarrow\ 5-(-2) = 7A$. Since two cells' voltages did not change, the duty cycle adjustment in a balanced system would not change based on (2). In the simulation, θ' remains the same value compared with previous condition in steady state, as shown by black line in the bottom plot of Fig. 10, which is consistent with the theoretical analysis above.

Switching to condition 3, due to inversed power requirement, the phase shift is controlled to be negative as expected from (7). Averaged leakage inductor current is decreased since $I_{cell1} - I_{cell2}$ is dropped from 7 A in condition 2 to 4 A in condition 3. The last condition verifies the C2C mode without power transferred to auxiliary power. It is a constant 5 A discharging from cell 1 and charging for cell 2. It is extremely beneficial if two cells in one HFB are unbalanced significantly. To clearly demonstrate the transient states, the zoom-ins of the beginning of each condition have been shown in Fig. 11. Generally speaking in each condition, the current references are followed properly and promptly. Therefore, the designed controllers are proved to be robust to manipulate control variables to achieve current requirements from global controllers.

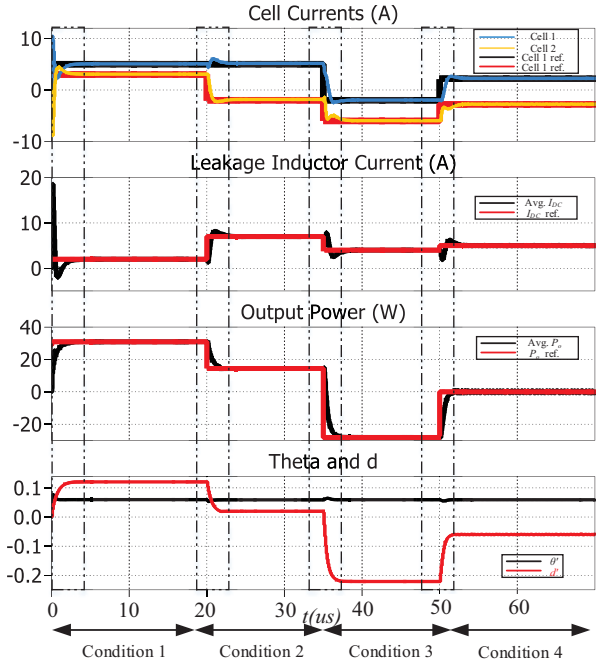

Fig. 10. Controller reactions to step reference changes

V. Conclusions

A HFB converter is applied in APM based balancing circuit, which allows the isolated power transfer from HV to LV as well as balancing two cell in one half bridge. The phase shift and duty cycle control are introduced to enable bi-direction power flow and balanced leakage inductor current. The average model of proposed HFB converter is derived and verified. A linearized and decoupled version of output power equation is given in terms of control variables d and θ by Taylor series expansion. To regulate the current from the cells in one HFB converter, PI controllers and PWM modulation are used to generate the necessary gate signals. The validation results show that the proposed average model is accurate to predict the dynamics of leakage inductance. Bode plots are applied as the tool to design the PI gains for the controllers. The controllers are also verified showing that the correct reference current can

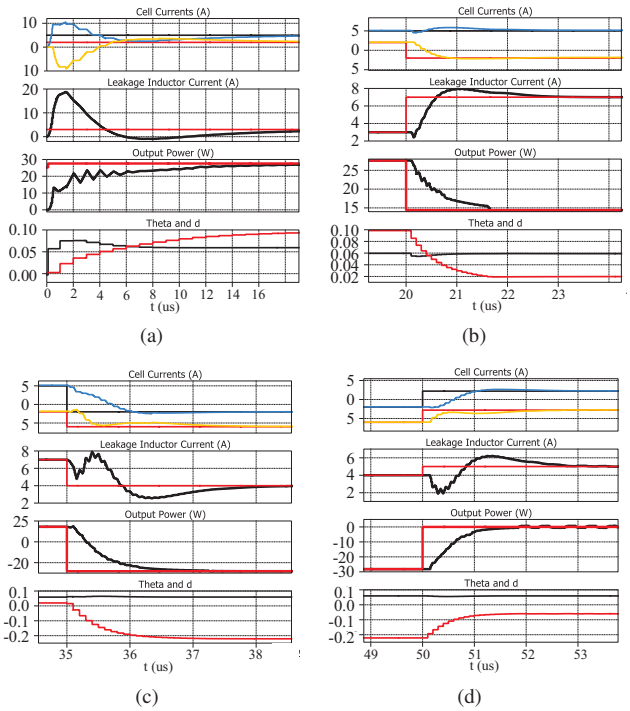

Fig. 11. Zoom-in plots (a) condition 1, (b) condition 2, (c) condition 3, (d) condition 4

be achieved rapidly. The test of reference change validates the robustness of the designed controllers.

In the future, the experimental validation will be conducted at 10 MHz switching frequency.

References

[1] B. Bilgin, P. Magne, P. Malysz, Y. Yang, V. Pantelic, M. Preindl, A. Korobkine, W. Jiang, M. Lawford, and A. Emadi, "Making the Case for Electrified Transportation," *IEEE Transactions on Transportation Electrification*, vol. 1, no. 1, pp. 4–17, jun 2015.

[2] J. Cao, N. Schofield, and A. Emadi, "Battery balancing methods: A comprehensive review," in *Vehicle Power and Propulsion Conference, 2008. VPPC '08. IEEE*. IEEE, 2008, pp. 1–6.

[3] L. McCurlie, M. Preindl, and A. Emadi, "Fast Model Predictive Control for Redistributive Lithium-Ion Battery Balancing," *IEEE Transactions on Industrial Electronics*, vol. 64, no. 2, pp. 1350–1357, feb 2017.

[4] M. Preindl, C. Danielson, and F. Borrelli, "Performance evaluation of battery balancing hardware," in *Control Conference (ECC), 2013 European*. IEEE, 2013, pp. 4065–4070.

[5] M. Preindl, "A Battery Balancing Auxiliary Power Module with Predictive Control for Electrified Transportation," *IEEE Transactions on Industrial Electronics*, vol. 0046, no. c, pp. 1–1, 2017.

[6] D. C. M. Evzelman, M. M. Ur Rehman, K. Hathaway, R. Zane and D. Maksimovic, "Active Balancing System for Electric Vehicles with Incorporated Low Voltage Bus," *IEEE Transactions on Power Electronics*, vol. 31, no. 11, pp. 7887–7895, nov 2016.

[7] F. Z. Peng, H. Li, G. J. Su, and J. S. Lawler, "A new ZVS bidirectional DC-DC converter for fuel cell and battery application," *IEEE Transactions on Power Electronics*, vol. 19, no. 1, pp. 54–65, 2004.

[8] R. T. Naayagi, A. J. Forsyth, and R. Shuttleworth, "High-power bidirectional DC-DC converter for aerospace applications," *IEEE Transactions on Power Electronics*, vol. 27, no. 11, pp. 4366–4379, 2012.

[9] A. Rodríguez, A. Vázquez, D. G. Lamar, M. M. Hernando, and J. Sebastián, "Different purpose design strategies and techniques to improve the performance of a dual active bridge with phase-shift control," *IEEE Transactions on Power Electronics*, vol. 30, no. 2, pp. 790–804, 2015.

[10] R. W. A. A. De Doncker, D. M. Divan, and M. H. Kheraluwala, "A Three-Phase Soft-Switched High-Power-Density DC/DC Converter for High-Power Applications," *IEEE Transactions on Industry Applications*, vol. 27, no. 1, pp. 63–73, 1991.

[11] R. W. Erick and D. Maksimovic, *Fundamentals of Power Electronics*, 2nd ed. KLUWER ACADEMIC PUBLISHERS, 2004.